Innovative thrust vectoring system with moveable jet vanes integrated with a moveable diffuser – Measurement and analysis of selected nozzle performance parameters

Łukasz K. NOCOŃ [1] [ORCID]*, Marta GRZYB [1], Piotr SZMIDT [1], and Łukasz M. NOWAKOWSKI [2]

[1] Kielce University of Technology, Department of Mechatronics and Armament Engineering, Faculty of Mechatronics and Mechanical Engineering, al. Tysiąclecia Państwa Polskiego 7, 25-314 Kielce, Poland

[2] Kielce University of Technology, Department of Mechanical Engineering and Metrology, Faculty of Mechatronics and Mechanical Engineering, al. Tysiąclecia Państwa Polskiego 7, 25-314 Kielce, Poland

Abstract. The aim of the study described herein was to design, construct and test a demonstrator of a system to control the direction of the resultant thrust vector of a rocket motor to be used in short range anti-tank missiles with a mass of up to 15 kg. The novelty of the system is that the direction of the resultant thrust vector is manipulated by means of moveable jet vanes integrated with a moveable nozzle diffuser through telescopic connectors. The technology demonstrator was built using different materials and different manufacturing processes. The first versions were 3D printed from plastic materials. Minor modifications to the design were made at an early stage. The final version had the main components made of aluminum using CNC machining. The system, with and without jet vanes, was tested on a specially developed test rig equipped with a multi-axis sensor to measure forces and torques. The nozzle performance parameters measured and analyzed in this study were the components of the thrust vector, the moments and the effective vectoring angle. The findings show that the experimental data are in good agreement with the results of earlier simulations and that the demonstrator is fully operational.

Keywords: anti-tank missile; thrust vectoring control; control actuation system; experimental testing.

1. INTRODUCTION

There are many different ways in which the direction of the resultant thrust vector can be manipulated in a rocket motor of an anti-tank guided missile. The methods may involve using a moveable nozzle diffuser, jet flaps, gas-dynamic gate rudders or jet vanes inside the exhaust space. Studies on the effectiveness of jet vane-based thrust vector control (JV-TVC) have been numerous, including those described in [1, 2]. Jet vanes acting as aerodynamic control surfaces cause the jet stream centerline to deflect from the longitudinal axis of the missile; thrust vectoring is achieved in this manner. The most popular approach to thrust vector control assumes that thrust loss can be reduced by increasing the nozzle divergence half-angle. The research discussed in [2] involved using a special mechanism of jet vanes to reduce thrust loss. Thrust vectoring phenomena were simulated using the Ansys Fluent software. The study included determining the mass flow rate of gas, one of the main parameters considered while analyzing thrust generation in the nozzle divergent section. In patent [3], a thrust vector control system with two pairs of jet vanes is employed to ensure a larger angle

of attack and greater maneuverability of a missile. The system allows each jet vane to rotate by an angle of up to ±30°, which prevents damage of the missile components in flight. Higher precision and reliability of the assembly can be achieved by modularizing it. The study described in [4] considered a JV-TVC system for an X-configuration missile. The major aim of the system was to shorten the missile free flight stage after the powered flight portion. For this missile configuration, a verified computational fluid dynamics (CFD) method was used. A special nonlinear mathematical model was developed for the TVC system integrated with an onboard missile guidance computer system.

Recently, greater interest has been taken in dual throat nozzles (DTNs), with this being a relatively new approach to thrust vectoring. One of the studies on the subject [5] involved calculations aimed at analyzing the performance of a DTN for different secondary mass flow rates. A new methodology for fluidic thrust vectoring, proposed in [6], takes into account the effects of chemical reactions, i.e. the influence of the reacting gas on flow parameters such as the separation point, reattachment point downstream and pressure distribution upstream the injection port.

Thrust vectoring can also be obtained by injecting fuel into the main jet stream of hot exhaust gases [7–9]. This method results in partially turbulent flow in the diffuser, which causes the

*e-mail: lukasn@tu.kielce.pl

Bull. Pol. Acad. Sci. Tech. Sci., vol. 72, no. 2, p. e148444, 2024

1

Ł.K. Nocoń, M. Grzyb, P. Szmidt, and Ł.M. Nowakowski

exhaust gas jet stream centerline to deflect. Extensive research into fluidic thrust vectoring methods for sonic and supersonic aeroengine exhausts has been carried out at the Propulsion Division of the CSIR National Aerospace Laboratories (NAL), India. Some of the latest developments in this area [10] include shock vector control and virtual aerodynamic internal surface shaping through nozzle throat skewing and separation control (dual throat and its variant with an immersed strut).

The maneuverability of a missile can be improved by combining different control actuator systems, as is the case of a Javelin anti-tank missile [11], which is equipped with four moveable jet vanes, four movable tail fins and eight fixed wings. A double control actuator system is also proposed in [12], but it does not involve thrust vectoring; the missile flight is controlled by aerodynamic control surfaces positioned before and after the center of gravity of the missile.

This article discusses a technology demonstrator of a moveable nozzle diffuser equipped with moveable jet vanes located inside the missile motor exhaust jet space. The solution, which is the first of this type, is described in a series of patent applications entitled "Rocket motor exhaust nozzle" [13–18]. The design of the thrust vector control system is based on a set of telescopic connectors responsible for proportional deflection of the jet vanes in relation to that of the nozzle diffuser. The demonstrator of the system used to control the direction of the resultant thrust vector was built with commercially available components and subassemblies, for example, servomechanisms, bearings, stretching screws, ball joints, rods and sleeves. The main parts of the system were made using two manufacturing processes: first 3D printing and then conventional machining. The additively manufactured demonstrator proved to be a fully functional, well-operating system. However, the design had to be validated before traditional machining was used. Obviously, the demonstrator construction was preceded by extensive computer simulations using a specially developed mathematical model.

2. DEMONSTRATOR DESIGN AND REDESIGN

The key assumption of the thrust vector control system was that the motion of the jet vanes would be proportional to that of the diffuser. There would thus be an angular relationship between these elements in an isosceles triangle, as illustrated in Fig. 1. The maximum angle of deflection of the jet vanes from the plane of symmetry of the diffuser, δ_j max, would be equal to the maximum angle of deflection of the diffuser from the plane of symmetry of the missile, δ_d max. As a result, the deflection of the jet vanes from the missile axis would be twice as great as the deflection of the diffuser. The jet vanes would be located inside the diffuser. They would be attached by means of telescopic connectors (segment AB in Fig. 1) to ensure that their deflection would be proportional to that of the diffuser.

The nozzle with a detachably connected nozzle throat insert is moveable because it is mounted on a gimbal-type joint with two bearings rotating about the lateral and vertical axes of the missile, which are also the axes of rotation of the nozzle. As a result, the jet stream centerline (the diffuser axis) can move
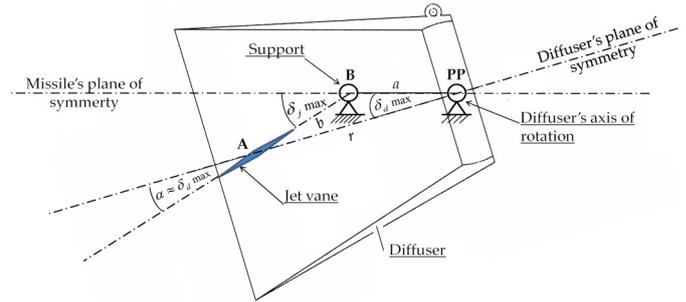

Fig. 1. Relative motion of the jet vanes and the rocket motor nozzle

smoothly in the exhaust space. The working space of the diffuser axis is a cone with an angle of about 16 deg ($2 \times \alpha$) and the apex located at the point of intersection of both axes of rotation of the nozzle. The outer ring of the gimbal-type joint forms part of the diffuser. Its role is to ensure thermal stability of the elements exposed to high temperatures. The use of a lower thermal conductivity material for the internal structure of the joint would reduce part of the heat generated at the joint. The inner gimbal ring is connected to the missile body, which is exposed to high temperatures.

The telescopic connectors allow one pair of vanes to move as needed, i.e. to deflect smoothly together with the diffuser. This does not mean that other vanes deflect in a different plane of motion. Figure 2 provides a graphic visualization of the thrust vector control system.
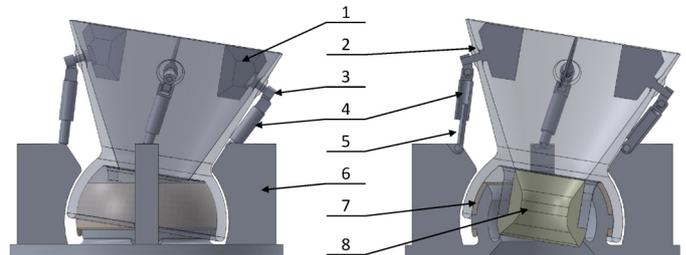

Fig. 2. Pictorial drawing of the thrust vector control system

The elements of the system depicted in Fig. 2 are: 1 – jet vane; 2 – nozzle diffuser; 3 – jet vane mount; 4 – upper part of the telescopic connector; 5 – lower part of the telescopic connector; 6 – missile body; 7 – central gimbal ring; 8 – diffuser throat insert.

The nozzle moves as a result of the synchronous operation of two servos. It is possible to mount another pair of servos if the torques generated by one pair of servos are too small to ensure efficient and fast operation of the system. Figure 3 shows a 3D assembly model of the first generation thrust vector control system.

The elements shown in Fig. 3 are as follows: 1 – jet vane; 2 – telescopic connector with the jet vane mount; 3 – diffuser; 4 – support to mount the telescopic connector; 5 – throat insert; 6 – lever to mount the ball joints; 7 – central ring of the gimbal-type joint; 8 – socket to seat the bearing responsible for one axis of rotation of the nozzle; 9 – MR 85 2RS bearing; 10 – ball
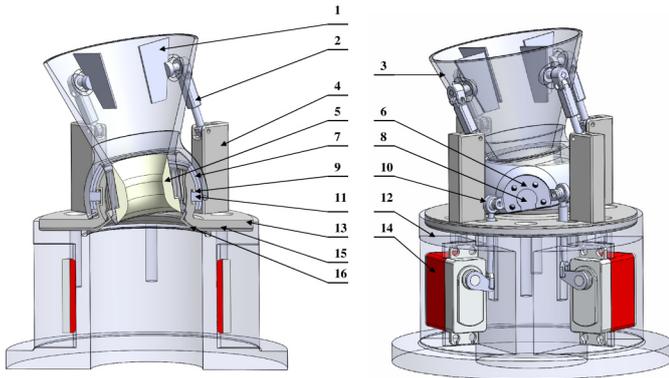
Fig. 3. Side view of the first generation thrust vector control system

joint connecting the moveable nozzle and the actuator; 11 – 5 mm diameter pin; 12 – missile body, 13 – frame of the inner ring of the gimbal-type joint with a socket to seat the bearing responsible for the other axis of rotation; 14 – servomechanism; 15 – heat insulation ring; 16 – elastic sealing cover plate.

The first version of the technology demonstrator of the thrust vector control system was 3D printed from VeroWhite using PolyJet Matrix (PJM) technology. Because of the limitations and requirements of this additive manufacturing method, the system design was modified. The mating elements required loose fits, so they were printed as subassemblies.

Figure 4 shows the arrangement of the parts on the build tray of the 3D printer, as simulated with the Objet Studio software. The parts were printed using a Stratasys Objet Connex350 printer.
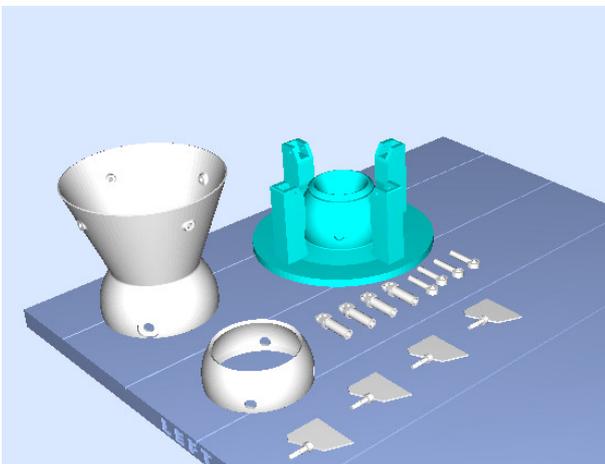

Fig. 4. View of an Objet Studio window

After printing, the support material was removed, the parts were cleaned with pressurized water and dried, and the demonstrator of the system for controlling the thrust vector was assembled (Fig. 5). The ball joints were printed as an integral part of the telescopic connector. The demonstrator was fully moveable because of the loose fits (0.2 mm) between the mating elements.

The first demonstrator (3D printed from VeroWhite) was developed to initially find out if the concept could succeed. The next version of the demonstrator was designed so that it would

Fig. 5. Early version of the demonstrator

be technically feasible to manufacture by CNC machining and to assemble using commercially available components and sub-assemblies (Fig. 6).
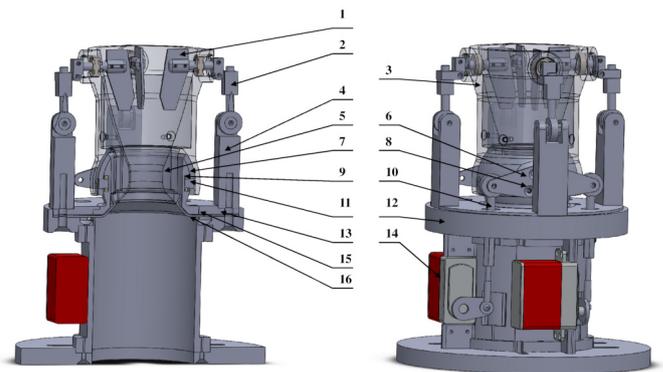

Fig. 6. Second generation demonstrator

The modifications were as follows:
1. The center of rotation of each jet vane (1) was moved so that the aerodynamic forces generated at the vane surface would partly compensate for the forces required to deflect both the diffuser and the jet vanes.
2. The telescopic connector (2) consisted of a 5 mm slide sleeve and a bronze internally threaded coupler to be screwed onto the M3 externally threaded bolt of the ball joint.
3. The nozzle with a detachably connected throat insert (1) was divided into three sections so that it would become easier to make using CNC machining.
4. The upper part of the diffuser had sockets to seat 619/5-2z rolling element bearings connected with the jet vane rollers to ensure the desired motion of the jet vanes.
5. The lever (6) was extended to increase the distance between the ball joint heads.
6. An MR 85 2RS bearing (9) was replaced with an MR 106 2RS bearing.
7. A 5 mm diameter pin (11) was replaced with a 6 mm diameter pin.

Bull. Pol. Acad. Sci. Tech. Sci., vol. 72, no. 2, p. e148444, 2024

3

8. The missile body (12) was represented by the base, tube and cover plate. Servo mounts were added.

9. Two servos (14) were used. They were commercially available FeeTech FT835BL servos.

10. The frame of the inner ring of the gimbal-type joint (13) had a socket to seat a bearing of the internal axis of rotation.

11. Each servo (14) was rotated by 180 degrees to increase the length of the stretching screw.

12. The support to mount the lower part of the telescopic connector (4) was rotated by 45 degrees to increase the distance between the heads of the ball joints.

13. The mounting of the servos was modified so that optionally four servos instead of two could be used to control the system.

3. DEMONSTRATOR CONSTRUCTION

The two final versions of the demonstrator differed in material and manufacturing process. In one (Fig. 7), most parts were 3D printed from MED610 using a Stratasys Objet Connex350 printer and some were made from PLA filament using a Maker-Bot FDM printer. After assembly, the demonstrator was fully functional. The other demonstrator had the main components made of aluminum using a Hermle B300 5-axis machining center.
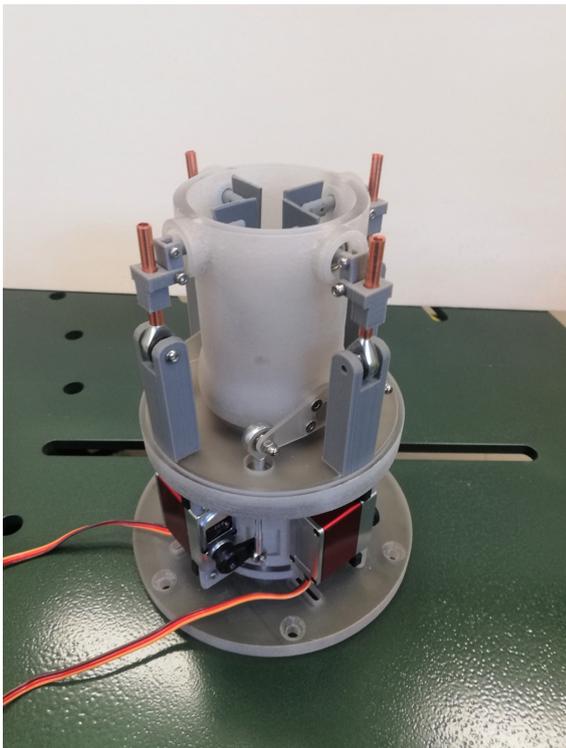

Fig. 7. Side view of the plastic demonstrator

3.1. 3D printed demonstrator

The tests were first conducted for the demonstrator containing nonmetallic components. The additively manufactured elements were: the pressure chamber body (Fig. 8), the central gimbal

ring (Fig. 9) and the elastic sealing cover plate. The strength parameters of the MED610 printing material were not determined prior to testing. The other parts were made of aluminum.
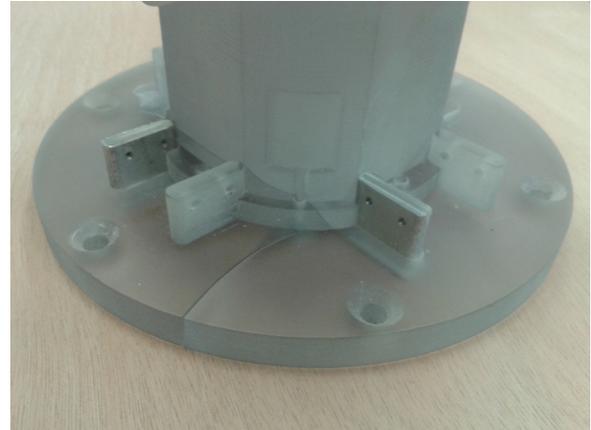
(a)

(b)

Fig. 8. (a), (b) Pressure chamber body which broke in testing

Fig. 9. Lubricated central gimbal ring before the demonstrator assembly

4

Bull. Pol. Acad. Sci. Tech. Sci., vol. 72, no. 2, p. e148444, 2024

The 3D printed demonstrator (containing composite elements) was tested at a pressure of 0.4 MPa. Under such conditions, the pressure chamber body (Fig. 8) and the central gimbal ring (Fig. 10) failed in testing.

Fig. 10. Central gimbal ring damaged in testing

The tests were then conducted for the demonstrator with CNC machined aluminum elements. The central gimbal ring with complex geometry was difficult to machine conventionally; the part was 3D printed as a split ring from PLA filament with a MakerBot FDM printer. The strength of the plastic gimbal ring was not sufficient; it broke in testing (Fig. 11).
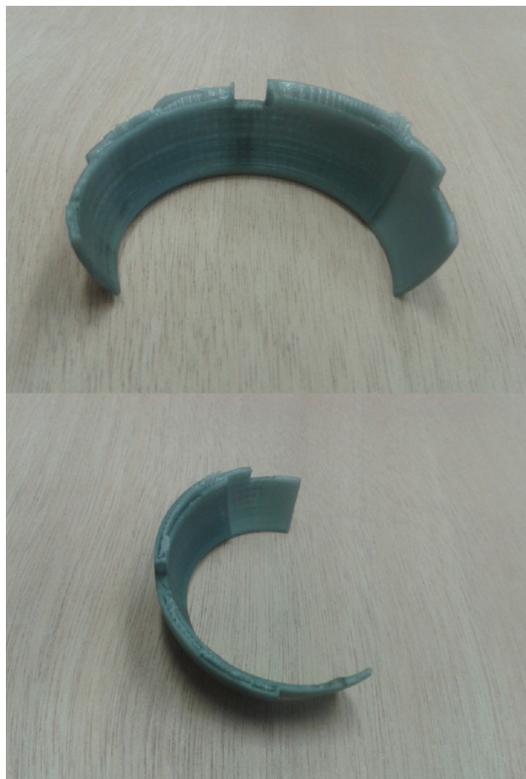
Fig. 11. Halves of the 3D printed PLA central gimbal ring damaged in testing

The air supplied at 0.4 MPa to the pressure chamber of the demonstrator generated a force of an order of 500 N acting on the moveable elements. The preliminary tests showed that elements 3D printed from PLA and MED610 were not suitable for prototyping purposes. Both materials are too brittle.

3.2. CNC machined demonstrator

The next step was to build a metallic demonstrator. All the nonmetallic elements were replaced with CNC machined parts made of aluminum (Fig. 13). The exception was the (split) central gimbal ring, which was first 3D printed from PLA filament (Fig. 12) and then CNC machined from steel (Fig. 13). Finally, a steel CNC machined ring was made.

Fig. 12. Aluminum demonstrator with a split central gimbal ring made of plastic prior to the assembly

Fig. 13. Aluminum demonstrator with a steel central gimbal ring prior to the assembly

Figures 14 and 15 display the metal demonstrator prior to testing. ' Figure 16 shows the orientation of the coordinate axes of the MCS10 multi-axis sensor.
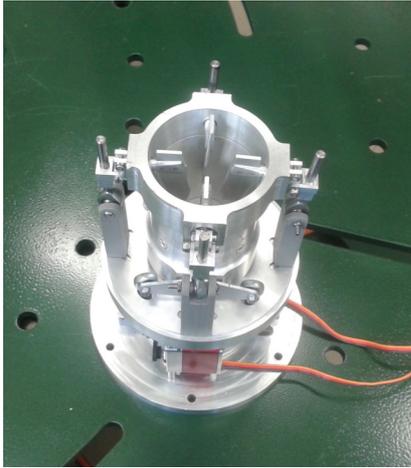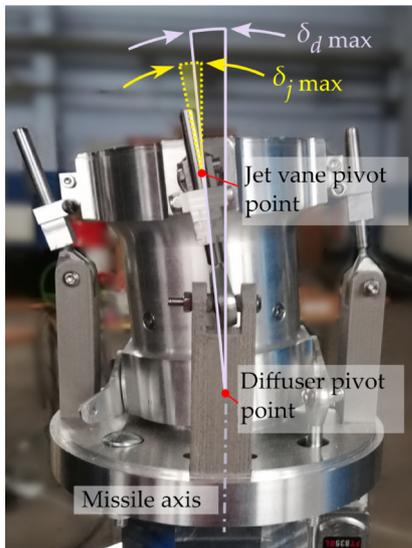
Fig. 14. Demonstrator before the tests

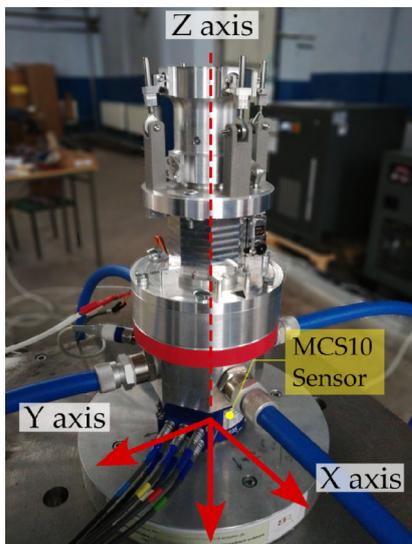**Fig. 15.** Metal demonstrator attached to the test rig

Fig. 16. Metal demonstrator attached to the test rig, orientations of the coordinate axes of the MCS10 multi-axis sensor

4. CONTROL MECHANISM FUNCTIONALITY TESTS

The main aim of the experiments was to find out how the demonstrator of the thrust vector control system would perform at different angular deflections of the jet vanes and the diffuser. The tests were carried out using a specially developed test rig equipped with an HBM MCS10 multi-axis sensor for monitoring forces and torques, an HBM P8AP pressure transducer, and an HBM MX840B measuring amplifier.

The experiments followed computer simulations based on a mathematical model described, for example, in [19–21]. The mathematical model was formulated for a hypothetical anti-tank guided missile (ATGM) with:

- initial mass of 13.287 kg;
- final mass of 8.7 kg (after missile propellant consumption);
- length of 1.2 m;
- diameter of 120 mm;
- velocity of 250 m/s.

An important part of the demonstrator design was thrust vectoring. The mathematical model used to describe the control forces generated by the motor nozzle was developed from formulae (1) and (2) describing the geometric relationships depicted in Fig. 17. For small angles (up to $\pm 10°$), approximated angular relationships were used.
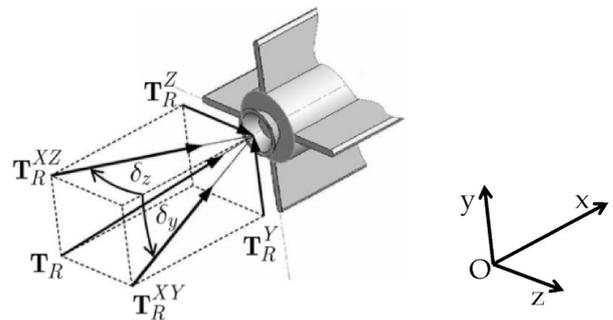

Fig. 17. Control forces generated by the deflection of the thrust vector control system

The symbols and designations used in Fig. 17 are:

$\mathbf{T}_R$ – motor thrust;
$\mathbf{T}_R^Y$ – thrust component along the vertical axis, Sy;
$\mathbf{T}_R^Z$ – thrust component along the horizontal axis, Sz;
$\mathbf{T}_R^X$ – thrust component along the longitudinal axis of the ATGM, Sx;
$\mathbf{T}_R^{XY}$ – thrust component in the vertical plane, Sxy;
$\mathbf{T}_R^{XZ}$ – thrust component in the horizontal plane, Sxz;
δ_z – angle of deflection of the thrust vector control system in the horizontal plane;
δ_y – angle of deflection of the thrust vector control system in the vertical plane.

Deflections of the rocket motor thrust vector relative to the longitudinal axis of symmetry of the ATGM by δ_y and/or δ_z (Fig. 17) generate control forces in both planes. The force controlling flight altitude $\mathbf{T}_R^Y$ is generated in the vertical plane, whereas the force controlling flight direction $\mathbf{T}_R^Z$ is generated in the plane perpendicular to the vertical plane passing through the missile's axis of symmetry [22].

6

Bull. Pol. Acad. Sci. Tech. Sci., vol. 72, no. 2, p. e148444, 2024

The relationships can be represented as trigonometric functions. It can thus be assumed that $T_R^X = T_R^{XZ} \cos \delta_z$ and $T_R^Z = T_R^{XZ} \sin \delta_z$ in the horizontal plane, Sxz, and $T_R^X = T_R^{XY} \cos \delta_y$ and $T_R^Y = T_R^{XY} \sin \delta_y$ in the vertical plane Sxy. The control forces T_R^Y and T_R^Z, derived in [22] are:
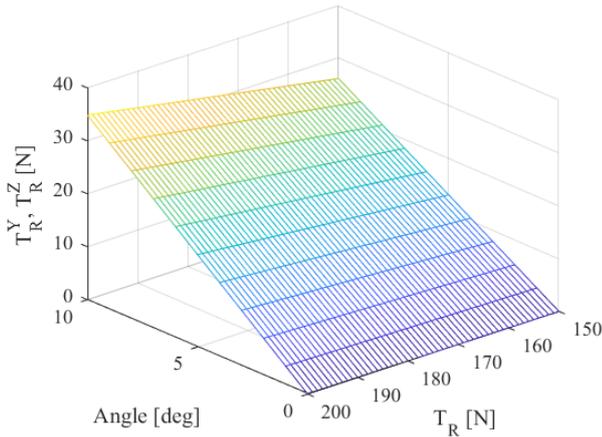
$$T_R^Y = \text{sgn}\left(\delta_y\right) \left| \mathbf{T}_R^Y \right|$$
$$= \text{sgn}\left(\delta_y\right) \sqrt{\frac{T_R^2 \cos^2 \delta_z \cdot \sin^2 \delta_y}{1 - \sin^2 \delta_z \cdot \sin^2 \delta_y}} \approx T_R \cdot \delta_y, \qquad (1)$$

$$T_R^Z = \text{sgn}\left(\delta_z\right) \left| \mathbf{T}_R^Z \right|$$
$$= \text{sgn}\left(\delta_z\right) \sqrt{\frac{T_R^2 \cos^2 \delta_y \cdot \sin^2 \delta_z}{1 - \sin^2 \delta_z \cdot \sin^2 \delta_y}} \approx T_R \cdot \delta_z. \qquad (2)$$

The z- and y-components of the thrust vector, T_R^Z and T_R^Y, respectively, are functions of two variables. At constant thrust T_R, they have the form of a linear function dependent on the effective vectoring angle. The functions are shown in Fig. 18.

Fig. 18. Components of the thrust vector versus the angle of deflection for different values of the resultant thrust

The tests performed on the demonstrator under laboratory conditions aimed to determine the real deflection of the resultant thrust vector from the missile axis in relation to the deflection of the thrust vector control system. The key elements of the system for controlling the resultant thrust vector are the diffuser and the jet vanes moving proportionally to each other. The angular deflection of the jet vanes is twice as large as that of the diffuser from the missile axis, reaching a maximum of about 16 deg. The maximum deflection of the diffuser is 8 deg. Figure 19 shows maximum deflections of the diffuser and jet vanes during testing. The deflections were set to be within a certain range by the control algorithm.

The tests conducted for the technology demonstrator helped detect and correct certain design flaws. For instance, the removal of the rubber vibration insulators from the servo mounts followed by servo calibration improved the system performance.

Two types of the system were considered: one with and the other without jet vanes inside the diffuser. They were tested at two inlet pressures of 0.8 MPa and 0.7 MPa.

Fig. 19. Maximum deflections of the diffuser and the jet vanes during testing

Figure 20 shows a solid model of the analyzed missile motor nozzle with the main geometric parameters.
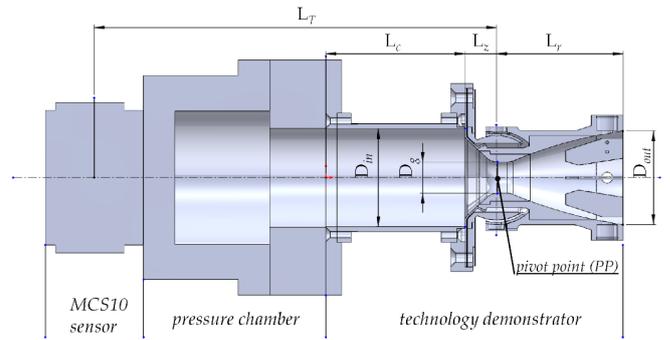
Fig. 20. Geometric model of the technology demonstrator

The main geometric dimensions of the demonstrator were:
- inlet diameter D_{in} = 62.50 mm,
- outlet diameter D_{out} = 60.00 mm,
- nozzle throat diameter D_g = 20 mm,
- combustion chamber length L_c = 88 mm,
- length of the convergent section of the nozzle L_z = 20 mm,
- length of the divergent section of the nozzle L_r = 80 mm,
- surface area of the jet vanes (area of control surfaces) S_T = 1800 mm^2 (4×450 mm^2 = 1800 mm^2),
- distance of the axis of rotation of the diffuser from the point of measurement (origin of the sensor coordinates) L_T = 254.5 mm.

The experimental results were used to determine the point of application of the resultant thrust vector and the effective vectoring angle for the proposed demonstrator. The effective vectoring angle is the angle of deflection of the jet stream centerline from the missile axis of symmetry:

$$\delta_v = \text{atan}\left(\frac{T_R^Y}{T_R^X}\right). \qquad (3)$$

In this article, the measurement data obtained during the tests will be provided in the form of moving averages of ten samples.

*Bull. Pol. Acad. Sci. Tech. Sci.*, vol. 72, no. 2, p. e148444, 2024

7

4.1. Measurement data for both types of demonstrator (i.e., with and without jet vanes) at inlet pressure of 0.8 MPa and maximum linear deflection

The experiments were performed for both types of the demonstrator, i.e. with and without jet vanes, at inlet pressure of 0.8 MPa. Each test lasted for 8 s. The measurement started at zero deflection from the vertical axis. The demonstrator was programmed to reach maximum deflection after about 5 s, which was kept constant for the next 2.7 s.

Figures 21 and 22 display the measurement data provided by the MCS10 sensor. As can be seen from Fig. 21, the deflection of the diffuser between the 4th and 9th seconds caused a significant decrease in the longitudinal thrust T_R^X, which was a result of the deflection of the resultant thrust vector from the demonstrator axis. From Fig. 21 and 22, it is clear that placing the jet vanes
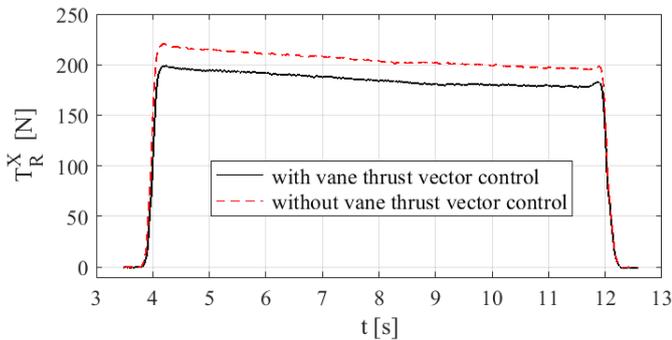

Fig. 21. X-component of the thrust vector (longitudinal thrust), $\mathbf{T}_R^X$, for the demonstrator with and without jet vanes (black solid and red dashed lines, respectively) subjected to a pressure of 0.8 MPa


(a)

(b)
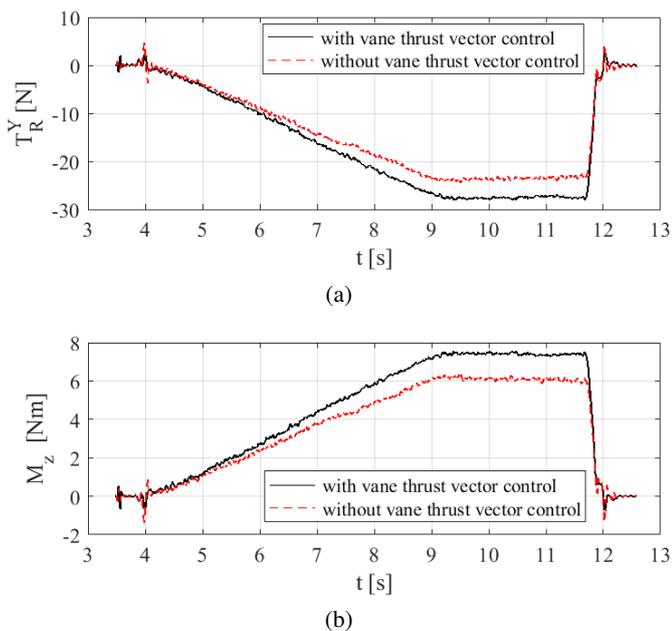
Fig. 22. Measurement results for both types of demonstrator: (a) Y-component of the thrust vector, $\mathbf{T}_R^Y$, being a force generated perpendicular to the longitudinal axis of the demonstrator; (b) moment about the z axis, $\mathbf{M}_Z$

inside the diffuser reduced the longitudinal thrust, T_R^X, which was due to a decrease in the cross-sectional area of gas flow and the occurrence of flow disturbances. Despite the losses of the longitudinal thrust by an average of 20 N (-10%), the lateral thrust (i.e. the control force), T_R^Y, increased by 15% (Fig. 22).

Figures 23 and 24 display the calculation data from the measurement results registered by the MCS10 sensor mounted on the test rig.
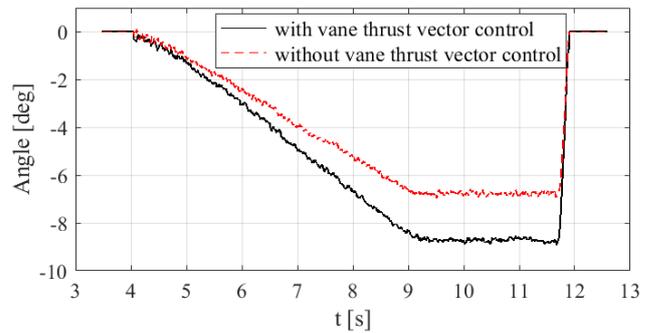
Fig. 23. Effective vectoring angle calculated from the test results
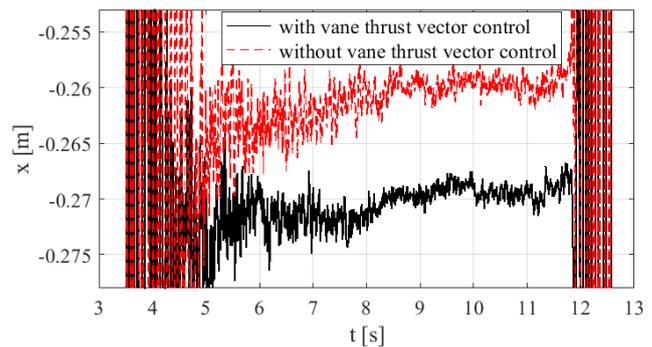
**Fig. 24.** Point of application of the resultant thrust vector calculated from the measurement results

In Fig. 23, the effective vectoring angle is plotted as a function of time. By contrast, Fig. 19 shows the actual angles of deflection of the thrust vector control system obtained in testing. Figure 24 depicts the point of application of the resultant thrust vector calculated using the formula for the moment about the z axis $M_Z = T_R^Y \cdot x$. For a system with jet vanes, the distance of this point from the origin of the sensor coordinates was approximately 270 mm. For a system without jet vanes, the point of application of the thrust vector was located closer to the axis of rotation of the diffuser, around 260 mm away from the point of measurement.

4.2. Measurement data for both types of demonstrator (i.e. with and without jet vanes) at inlet pressure of 0.7 MPa and maximum linear deflection

The tests performed for the demonstrator with and without jet vanes at inlet pressure of 0.7 MPa were 8 s in duration. Each measurement started with a zero effective vectoring angle, i.e. at

8

*Bull. Pol. Acad. Sci. Tech. Sci.*, vol. 72, no. 2, p. e148444, 2024

zero deflection of the resultant thrust vector from the longitudinal axis. Maximum deflection of the demonstrator was reached after about 5 s and remained unchanged for the next 2.7 s. The diagrams in Fig. 25 and 26 show the measurement data obtained for the demonstrator subjected to inlet pressure of 0.7 MPa.
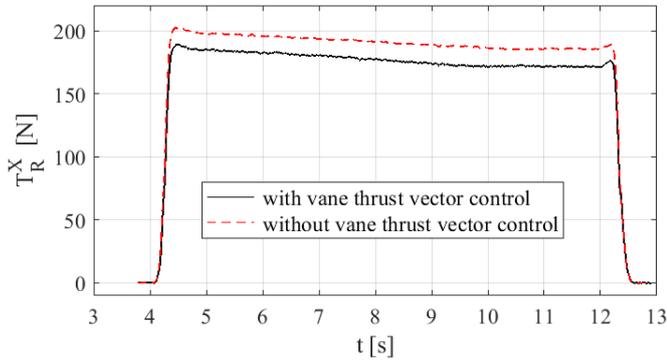
Fig. 25. Measurement data obtained at a working pressure of 0.7 MPa: the x-component of the thrust vector (longitudinal thrust), $\mathbf{T}_R^X$ for the demonstrator with and without jet vanes (in black and red, respectively)
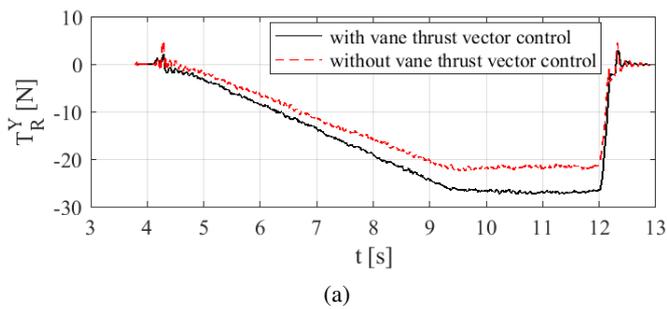
(a)
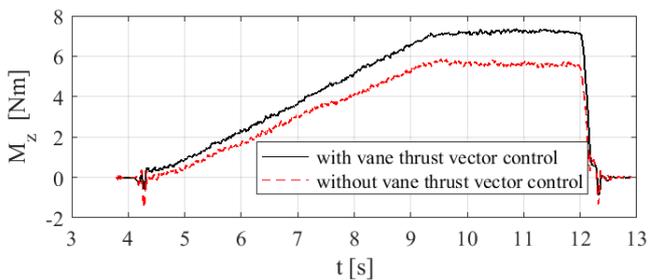
(b)

Fig. 26. Measurement results obtained at a pressure of 7 MPa: (a) y-component of the thrust vector, $\mathbf{T}_R^Y$, being the control force generated perpendicular to the longitudinal axis of the demonstrator; (b) moment about the z axis, $\mathbf{M}_Z$

From Fig. 25 and 26, it is clear that placing the jet vanes inside the diffuser reduced the longitudinal thrust, $\mathbf{T}_R^X$, which was due to a decrease in the cross-sectional area of gas flow and the occurrence of flow disturbances. Despite the losses of the longitudinal thrust by an average of 15 N, the lateral thrust (i.e. the control force), $\mathbf{T}_R^Y$, increased by 20% (5 N) (Fig. 26).

Figures 27 and 28 illustrate the effective vectoring angle and the point of application of the resultant thrust vector, respectively.
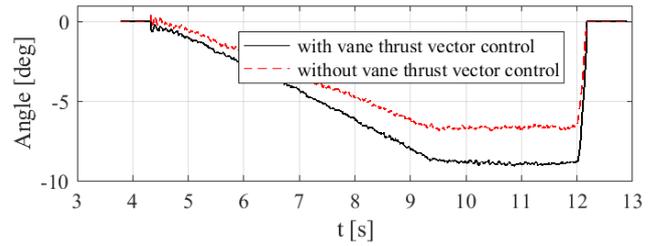

Fig. 27. Effective vectoring angle determined from the test data
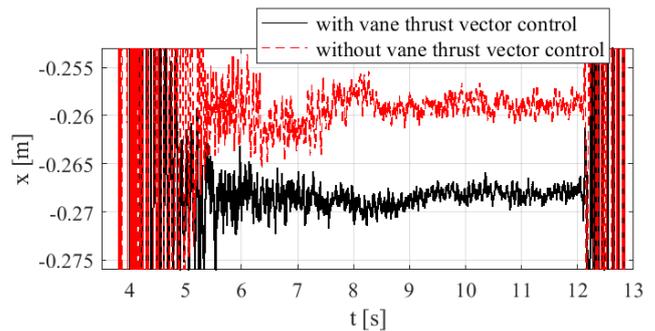
**Fig. 28.** Point of application of the resultant thrust vector

The point of application of the resultant thrust vector was calculated from the formula for the moment about the z axis: $M_Z = T_R^Y \cdot x$.

Figures 29 and 30 show the location of the resultant thrust vector, its point of application, and the effective vectoring angle (angle of deflection of the jet stream centerline from the missile axis).
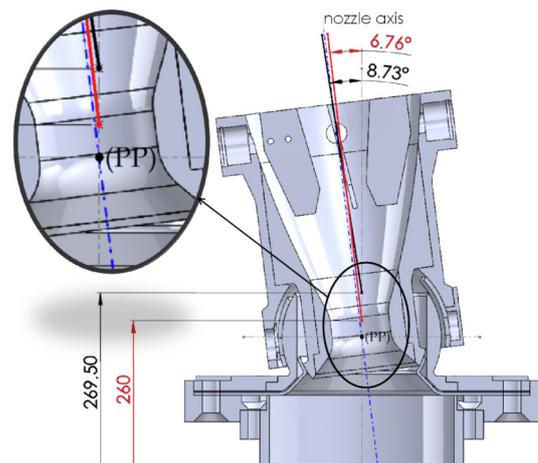
Fig. 29. Location of the resultant thrust vector and the effective vectoring angle at a pressure of 0.8 MPa for a system with and without jet vanes (in black and red, respectively)

There were considerable disturbances due to the startup and shutdown of the test rig around the 4th and 12th seconds, respectively. These, however, had little effect on the measurement results; they were omitted when calculating the resultant thrust.

Ł.K. Nocoń, M. Grzyb, P. Szmidt, and Ł.M. Nowakowski
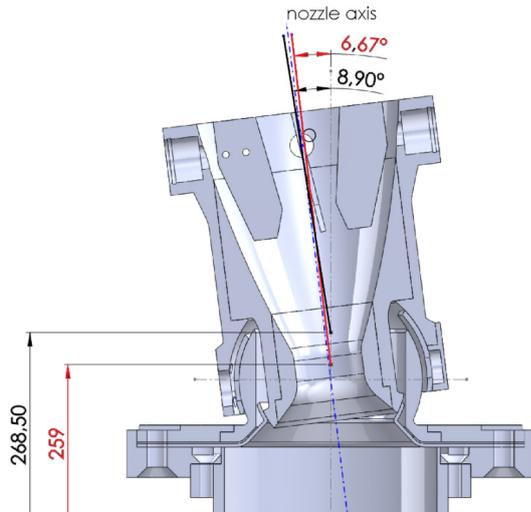
Fig. 30. Location of the resultant thrust vector and the effective vectoring angle at a pressure of 0.7 MPa for a system with and without jet vanes (in black and red, respectively)

5. CONCLUSIONS

The research described in this article was concerned with a technology demonstrator of a thrust vector control system for an anti-tank guided missile. The main objective was to check whether the system would operate effectively under test conditions similar to real conditions. The experimental data obtained for two types of the demonstrator (i.e. with and without jet vanes) were in good agreement with the simulation results. The system can be used in a variety of scenarios where the ability to move the diffuser is limited, e.g. due to design constraints or when maintaining aerodynamic performance is required.

The measurement data analysis revealed that when missile maneuverability was taken into consideration, the system equipped with jet vanes was more effective than the one without them. Despite the fact that the thrust along the x axis was smaller for the system with jet vanes, the side control forces generated by the deflecting diffuser were greater.

Compressed air was used as a replacement for the exhaust gases from rocket propellant to achieve the required thrust. This testing solution was cheaper, safer and better for the environment.

Further research is required to analyze measurement errors that may occur while determining the thrust vector and the angular deflection of the proposed system. Simulations and tests would be essential for different nozzle throat diameters (critical cross-sections) and different geometries of the jet vanes to improve the effectiveness of the proposed thrust vector control system and, consequently, to achieve enhanced maneuverability and performance of a missile.

REFERENCES

[1] M.S.R.C. Murty, M.S. Rao, and D. Chakraborty, "Numerical simulation of nozzle flow field with jet vane thrust vector control," *J. Aerosp. Eng.*, vol. 224, pp. 541–548, 2009, doi: 10.1243/09544100JAERO677.

[2] D. Daljit Majil, M. Saleem, and S. Kumaresan, "Computational study on reduction of thrust loss in jet vane thrust vectoring nozzle,". *Int. J. Aerosp. Mech. Eng.*, vol. 3, no. 5, pp. 1–6, 2016.

[3] W.-H. Kim, J.-Ch. Bae, S.-T. Lim, and S.-H. Park, "Jet vane thrust vector control system," U.S. Patent US007313910B2, Jan. 1, 2008.

[4] M.S.R.C. Murty and D. Chakraborty, "Numerical Characterisation of Jet-Vane based Thrust Vector Control Systems," *Def. Sci. J.*, vol. 65, no. 4, pp. 261–264, 2015, doi: 10.14429/dsj.65.7960.

[5] C.S. Shin and H.D. Kim, "A Fundamental Study of Thrust-Vector Control Using a Dual Throat Nozzle," Proc. *Spring Conference 2010 of the Korean Society of Propulsion Engineering,* 2010, pp. 339–342.

[6] R. Chouicha, M. Sellam, and S. Bergheul, "Effect of chemical reactions on the fluidic thrust vectoring of an axisymmetric nozzle," *Int. J. Aviat. Aeronaut. Aerosp.*, vol. 5, no. 5, pp. 1–15, 2019, doi: 10.15394/ijaaa.2019.1377.

[7] S. Forde, M. Bulman, and T. Neill, "Thrust augmentation nozzle (TAN) concept for rocket engine booster applications," *Acta Astronaut.*, vol. 59, pp. 271–277, 2006, doi: 10.1016/j.actaastro.2006.02.052.

[8] E. Resta, R. Marsilio, and M. Ferlauto, "Thrust Vectoring of a Fixed Axisymmetric Supersonic Nozzle Using the Shock-Vector Control Method," *Fluids*, vol. 6, p. 441, 2021, doi: 10.3390/fluids6120441.

[9] V. Zmijanovic, V. Lago, L. Léger, E. Depussay, M. Sellam, and A. Chpoun, "Thrust vectoring effects of a transverse gas injection into a supersonic cross flow of an axisymmetric convergent-divergent nozzle," *Prog. Propuls. Phys.*, vol. 4, pp. 227–256, 2013, doi: 10.1051/eucass/201304227.

[10] J.J. Isaac and C. Rajashekar, "Fluidic thrust vectoring nozzles," Propulsion Division National Aerospace Laboratories (Council of Scientific & Industrial Research), Bangalore 560017, India, 2014. [Online]. Available: https://core.ac.uk/download/pdf/151646399.pdf

[11] J. Harris and N. Slegers, "Performance of a fire-and-forget anti-tank missile with a damaged wing," *Math. Comput. Model.*, vol. 50, pp. 292–305, 2009, doi: 10.1016/j.mcm.2009.02.009.

[12] W. Bużantowicz and J. Pietrasieński, "Dual-control missile guidance: A simulation study," *J. Theor. Appl. Mech.*, vol. 56, no. 3, pp. 727–739, 2018, doi: 10.15632/jtam-pl.56.3.727.

[13] M. Grzyb, Ł. Nocoń, Ł. Nowakowski, and P. Szmidt, "Rocket motor exhaust nozzle," PL Patent Pat.241948, filed 4 June 2020, and issued 13 October 2022.

[14] M. Grzyb, Ł. Nocoń, Ł. Nowakowski, and P. Szmidt, "Rocket motor exhaust nozzle," PL Patent Pat.241949, filed 4 June 2020, and issued 13 October 2022.

[15] M. Grzyb, Ł. Nocoń, Ł. Nowakowski, and P. Szmidt, "Rocket motor exhaust nozzle," PL Patent Pat.241946, filed 4 June 2020, and issued 13 October 2022.

[16] M. Grzyb, Ł. Nocoń, Ł. Nowakowski, and P. Szmidt, "Rocket motor exhaust nozzle," PL Patent Pat.241947, 13 October 2022.

[17] M. Grzyb, Ł. Nocoń, Ł. Nowakowski, and P. Szmidt, "Rocket motor exhaust nozzle," PL Patent Pat.241945, 12 October 2022.

[18] M. Grzyb, Ł. Nocoń, Ł. Nowakowski, and P. Szmidt, "Rocket motor exhaust nozzle," PL Patent Pat.241969, 17 October 2022.

[19] Z. Koruba and Ł. Nocoń, "Modified linear-quadratic regulator used for controlling anti-tank guided missile in vertical plane," *J. Theor. App. Mech.*, vol. 58, pp. 723–732, 2020, doi: 10.15632/jtam-pl/122205.

[20] Ł. Nocoń, M. Grzyb, P. Szmidt, Z. Koruba, and Ł. Nowakowski, "Control Analysis with Modified LQR Method of Anti-Tank Missile with Vectorization of the Rocket Engine Thrust," *Energies,* vol. 15, no. 1, p. 356(1–17), 2022, doi: 10.3390/en15010356.

[21] Ł. Nocoń and Z. Koruba, "Modification of control actuation systems of ATGM," in Proc. *23rd International Conference on Engineering Mechanics*, Czech Republic, 15-18 May 2017, pp. 714–717.

[22] Z. Koruba and Ł. Nocoń, "Optimal Compensator for Anti-Ship Missile with Vectorization of Engine Thrust," *Appl. Mech. Mater.*, vol. 817, pp. 279–288, 2016, doi: 10.4028/www.scientific.net/AMM.817.279.